AIP | Physics of Fluids

Dissipative-particle dynamics simulations of flow over a stationary sphere in compliant channels

Harinath Reddy and John Abraham

Citation: Phys. Fluids **21**, 053303 (2009); doi: 10.1063/1.3134044
View online: http://dx.doi.org/10.1063/1.3134044
View Table of Contents: http://pof.aip.org/resource/1/PHFLE6/v21/i5
Published by the American Institute of Physics.

Dissipative-particle dynamics simulations of flow over a stationary sphere in compliant channels

Harinath Reddy and John Abraham
School of Mechanical Engineering, Purdue University, West Lafayette, Indiana 47907, USA

(Received 7 November 2008; accepted 1 April 2009; published online 13 May 2009)

Dissipative-particle dynamics (DPD), a particle-based fluid-simulation approach, is employed to simulate isothermal pressure-driven flow across a sphere in compliant cylindrical channels. The sphere is represented by frozen DPD particles, while the surrounding fluid is modeled using simple fluid particles. The channel walls are made up of interconnected finite extensible nonlinear elastic bead-spring chains. The wall particles at the inlet and outlet ends of the channel are frozen so as to hinge the channel. The model is assessed for accuracy by computing the drag coefficient C_D in shear flow past a uniform sphere in unbounded flow, and comparing the results with those from correlations in literature. The effect of the aspect ratio λ of the channel, i.e., the ratio of the sphere diameter d to the channel diameter D, on the drag force $\mathbf{F}_D$ on the sphere is investigated, and it is found that $\mathbf{F}_D$ decreases as λ decreases toward the values predicted by the correlations as λ approaches zero. The effect of the elasticity of the wall is also studied. It is observed that as the wall becomes more elastic, there is a decrease in $\mathbf{F}_D$ on the sphere. © *2009 American Institute of Physics*.
[DOI: 10.1063/1.3134044]

I. INTRODUCTION

Simulating fluid flow in compliant channels at micro- and submicron scales, e.g., microcapillaries, is computationally challenging because of the difficulty of representing dynamically deforming surfaces. Furthermore, interesting elements of the physics, e.g., slip at walls and effects arising from thermal fluctuations, may not be captured by continuum methods. In principle, molecular dynamics (MD) can be used to capture all the flow features, but it is computationally impractical beyond nanoscales. Various methods such as lattice gas automata,[1,2] lattice Boltzmann methods (LBMs),[3] and finite-element methods[4] have been proposed and applied for studying fluid-structure interaction. These methods, especially LBM, have been utilized with some success to simulate various microscale phenomena.[5,6] However, the drawback of lattice methods is that the representation of the dynamically deforming boundary by the lattice[3] can be difficult.

Dissipative-particle dynamics (DPD), developed by Hoogerbrugge and Koelman,[7] is a particle-based numerical method which has shown promise in the simulation of complex fluid dynamical phenomena. Each DPD particle can be conceptually viewed as a collection of atoms/molecules. Since the atomistic details are lost in the process of generating the particles, the method can be viewed as coarse-grained MD. The coarse graining of particles leads to an interparticle force which has a soft-core potential, i.e., it does not exceed a maximum value. It can be shown that the macroscopic conservation equations can be derived from the DPD equations of motion by solving the Fokker–Planck equation.[8,9] Hence, DPD can be employed to simulate continuum phenomena in addition to flows at the submicron scale. This makes the method a powerful tool for solving problems over a wide range of length and time scales. It has been successfully employed to simulate colloidal suspensions,[10] polymer solutions,[11] binary immiscible fluids,[12] and drops in shear flow.[13] It has also been utilized to simulate multiphase phenomena at submicron scales, such as the breakup of liquid nanocylinders[14] and liquid nanojets.[15] What makes the method attractive for the problem of interest in this work is that it can also be adapted to simulate complex boundaries.

Hoogerbrugge and Koelman[7] employed DPD to investigate flow across a sphere using DPD, and estimated the dimensionless drag coefficient for suspensions of solid spheres with concentrations of 10%–30% under creeping flow conditions. They also studied the flow of such suspensions under steady shear flow. The computed viscosities for systems up to 35% volume fraction of solid suspension showed good agreement with existing experimental and numerical studies. Boek and van der Schoot[16] studied the rheology of dense particulate suspensions of spheres, disks, and rods using DPD, and studied the dependence of fluid viscosity on the volume fraction of suspension particles and shear rates. Dzwinel and Yuen[17] carried out simulations of colloidal structures at various scales utilizing a smooth-sphere model and discussed a multiscale approach to carry out simulations of colloidal suspensions over a wide range of scales. Whittle and Dickinson[18] modeled colloidal systems using spherical particles and developed a modified DPD model with a central core. These prior studies have focused on flow across a suspension of particles and are constrained to the low Reynolds number (Re) regime, i.e., $\mathrm{Re} < 1$. The Re is defined based on the diameter of the sphere. There is still a need to study the dynamics of single particle and the effect of bulk properties on fluid-structure interaction over a wider range of Re. Note that while microchannels typically operate at low Re, there are systems where higher Re is important, e.g.,

micropumps, small blood vessels. Furthermore, DPD is not restricted to flow in microchannels.

Recently, Kim and Phillips[19] utilized DPD to study flow over cylinders and spheres for Re in the range of 0.1–200. They computed the drag coefficient, C_D, and presented qualitative comparisons with predictions from theoretical correlations and experimental results, and reported excellent agreement up to Re=100 beyond which compressibility effects cause discrepancies. Chen *et al.*[20] carried out simulations of flow over spheres in domains where periodic boundary conditions were employed in the streamwise direction. As in the work of Kim and Phillips, they utilized a rough-sphere model where the sphere was represented by frozen particles. They pointed out that the periodic images of the spheres do not influence the flow field of each other if the boundaries are sufficiently far apart. They also concluded, like Kim and Phillips, that compressibility effects which become important at Re$>$100 can cause deviation of computed C_D from theoretical predictions.

In the present work, the approach used by Chen *et al.*[20] will be extended to carry out simulations in bounded flow across a sphere in *cylindrical compliant channels*. The studies in Refs. 19 and 20 were in rectangular channels with rigid walls. The sphere diameter d to channel diameter D aspect ratio λ has a significant effect on the drag force imposed on the sphere. The effects of λ on C_D will be studied for a range of Re. An interconnected finite extensible nonlinear elastic (FENE) chain bead-spring model[21] is employed to model the compliant walls. The effect of the wall elasticity on C_D and the hydrodynamic behavior of the system will be analyzed. This paper is organized as follows: In Sec. II an overview of the DPD model, FENE chain bead-spring model, and the sphere model is provided. The implementation of the DPD model is discussed in Sec. III. Section IV presents the results and discussion. The conclusions of this paper are summarized in Sec. V.

II. THE DPD MODEL

In this section, an overview of the DPD model will be provided. Details of the model and its theoretical framework can be found in Refs. 7, 22, and 23. The DPD system consists of coarse-grained particles which represent clusters of molecules. The time evolution of the position and velocity of a DPD particle i of unit mass are computed from Newton's laws of motion given by

$$\frac{d\mathbf{r}_i}{dt} = \mathbf{v}_i, \qquad \frac{d\mathbf{v}_i}{dt} = \mathbf{f}_i, \tag{1}$$

where $\mathbf{r}_i$, $\mathbf{v}_i$, and $\mathbf{f}_i$ denote the position, velocity, and force vectors, respectively. The mass of all the particles is set to unity so that the force acting on a particle is equal to its acceleration. The force on a particle arises from interparticle interactions. This force has four components, three of which are pairwise additive, i.e.,

$$\mathbf{f}_i = \sum_{i \neq j} (\mathbf{F}_{ij}^C + \mathbf{F}_{ij}^D + \mathbf{F}_{ij}^R) + \mathbf{F}_{\text{ext}}, \tag{2}$$

where $\mathbf{F}_{ij}^C$, $\mathbf{F}_{ij}^D$, and $\mathbf{F}_{ij}^R$ represent the conservative, dissipative, and random components of the force, respectively, and the summation is carried out over all other particles within a cutoff radius r_c. $\mathbf{F}_{\text{ext}}$ represents the external forces that are acting on the system. Since this is the only length scale in the system, the cutoff radius is used as the unit of length, i.e., $r_c=1$.

The conservative force component $\mathbf{F}_{ij}^C$ between particles i and j accounts for the configurational energy of the system and represents its nonideality. It is responsible for the thermodynamic behavior of the system. The dissipative force component $\mathbf{F}_{ij}^D$ is responsible for the viscous effects in the DPD system and it tends to reduce the relative velocity between any two particles in an interacting pair. As a result the system temperature will reduce. The random force $\mathbf{F}_{ij}^R$ can be understood as follows: At the molecular level there are many collisions that take place between the actual atoms/molecules. However, when a group of atoms/molecules is represented by a DPD particle, there is a reduction in the number of collisions. The force $\mathbf{F}_{ij}^R$ accounts for the degrees of freedom "lost" during the coarse-graining process. It "heats" the DPD system as it supplies energy to the interacting particles. If $\mathbf{F}_{ij}^D$ and $\mathbf{F}_{ij}^R$ are balanced, an isothermal system will result. The dissipative and random forces are responsible for the hydrodynamic behavior of the DPD system. The functional forms of the interparticle forces between particles i and j are given by

$$\mathbf{F}_{ij}^C = \begin{cases} a_{ij}(1 - r_{ij}/r_c)\mathbf{e}_{ij}, & (r_{ij} < r_c), \\ 0, & (r_{ij} \geq r_c), \end{cases} \tag{3}$$

$$\mathbf{F}_{ij}^D = -\gamma\omega^D(r_{ij})(\mathbf{e}_{ij} \bullet \mathbf{v}_{ij})\mathbf{e}_{ij}, \tag{4}$$

and

$$\mathbf{F}_{ij}^R = \sigma\omega^R(r_{ij})\xi_{ij}\mathbf{e}_{ij}. \tag{5}$$

Here, $\mathbf{e}_{ij}$ is a unit vector given by $\mathbf{e}_{ij}=\mathbf{r}_{ij}/|\mathbf{r}_{ij}|$, where $\mathbf{r}_{ij}=\mathbf{r}_i-\mathbf{r}_j$, $\mathbf{v}_{ij}=\mathbf{v}_i-\mathbf{v}_j$, γ is the amplitude of the dissipative force, σ is the amplitude of random force, ω^D and ω^R are the weight functions for the dissipative and random force, respectively. Since DPD is a short-range model, the weight functions are chosen such that their values go to zero beyond the cutoff distance, i.e., each particle interacts only with particles which are within the cutoff distance. The term ξ_{ij} in Eq. (5) is a random variable which has zero mean, unit variance, and is uncorrelated in time. It follows Gaussian statistics and has the following properties:

$$\langle \xi_{ij}(t) \rangle = 0, \qquad \langle \xi_{ij}(t)\xi_{kl}(t') \rangle = (\delta_{ik}\delta_{jl} + \delta_{il}\delta_{jk})\delta(t-t'). \tag{6}$$

Espanol and Warren,[22] by applying the fluctuation-dissipation theorem to the DPD system, showed that the Gibbs equilibrium distribution is recovered from the model. The application of the fluctuation-dissipation theorem to the

DPD system gives the following relationship between the amplitudes and the weight functions of the dissipative and random forces:

$$\omega^D(r) = [\omega^R(r)]^2, \quad \sigma^2 = 2\gamma k_B T. \tag{7}$$

In this work, the following functional form for the weight functions in the expressions for the dissipative and random forces have been chosen:

$$\omega^D(r) = [\omega^R(r)]^2 = \begin{cases} \left(1 - \frac{r}{r_c}\right)^2, & (r < r_c), \\ 0, & (r \geq r_c). \end{cases} \tag{8}$$

Notice that these weight functions depend on the interparticle separation r and the cutoff radius r_c. This paper utilizes a traditional quadratic weighting scheme instead of the weight functions employed by Chen *et al.*[20]

The DPD equations of motion are integrated using a modified-Verlet scheme proposed by Groot and Warren,[23] and used in several prior studies.[14,15,20,21,24] The time step Δt used to integrate the velocity Verlet algorithm is 0.01. This time step has been selected in accordance with the discussion of choice of time step in Ref. 23. Thermal and viscous time scales can be defined for the simulation. The thermal time scale τ_{th} is given by

$$\tau_{\text{th}} = \frac{\sqrt{k_B T}}{r_c}, \tag{9}$$

where $k_B T$ is the system temperature and r_c is the cutoff radius (length scale of the system). The thermal time scale for the simulations in this work is 1. A viscous time scale τ_{vis} can also be defined as the ratio of the square of channel width W and the kinematic viscosity υ, i.e.,

$$\tau_{\text{vis}} = \frac{W^2}{\upsilon}. \tag{10}$$

The channel width (or diameter for cylindrical channels) is of the order ~13 DPD units and viscosity is ~0.27. Hence the viscous time scale has the $O(500)$. Since Δt is much smaller than either of the time scales mentioned above, the physics is resolved accurately. This was confirmed by repeating the computation with $\Delta t = 0.005$.

A. FENE chain model

Various models have been proposed in the literature to describe the elastic behavior of walls. One model that is widely employed to model the elasticity observed in polymers is the FENE bead-spring chain model.[11] The model is designed to mimic a non-Newtonian fluid. This model is adapted to simulate the elastic behavior of channel walls in the present study. The FENE rheology and conformational changes under shear are well documented in literature.[11,21] A chain of bead-and-spring particles is constructed, as shown in Fig. 1(a), by joining a series of DPD wall particles with a spring that has a nonlinear elastic behavior.

In the present study, various such chains are cross-linked using nonlinear elastic springs to form an elastic boundary wall, as shown in Fig. 1(b). The black wall particles are stationary and act as an anchor to the rest of the wall while all other particles are allowed to move. The elastic behavior of the wall is modeled by adding an additional component to the force between the wall particles. The net force acting on a wall particle is

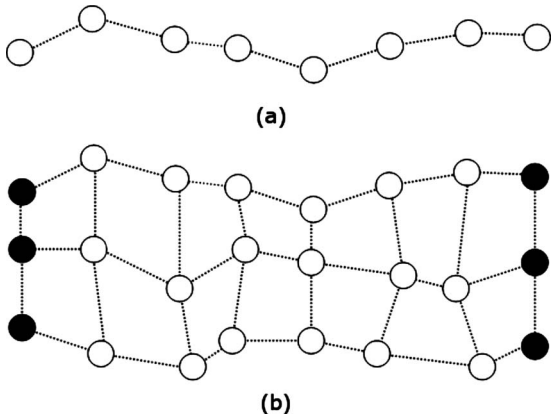

FIG. 1. (a) FENE bead-chain spring. (b) Elastic wall modeled using cross-linked FENE bead-chain springs.

$$\mathbf{f}_i = \underbrace{\sum_{i \neq j} \mathbf{F}_{ij}^C + \mathbf{F}_{ij}^D + \mathbf{F}_{ij}^R}_{I} + \underbrace{\sum_{i \neq j} \mathbf{F}_{ij}^C + \mathbf{F}_{ij}^D + \mathbf{F}_{ij}^R + \mathbf{F}_{ij}^S}_{II}, \tag{11}$$

where the first set of terms (I) is the force applied by the fluid particles on the ith wall particle and the second set of terms (II) is the force applied by the surrounding wall particles on the ith wall particle. Notice from Eq. (11) that the surrounding wall particles apply an additional force, the spring force $\mathbf{F}_{ij}^S$. In FENE chains,[21] the spring force applied on particle i due to particle j is

$$\mathbf{F}_{ij}^S = \frac{H r_{ij}}{1 - (r_{ij}/r_{\max})^2}, \tag{12}$$

where H is the spring constant, whose values are given later in the paper where the model is used, and $r_{\max}$ is the maximum permissible length of one chain segment. The spring force increases drastically with increasing r_{ij}/r_m and becomes infinitely large as r_{ij}/r_m approaches unity. This model can capture the finite extensibility of the wall. The mass of the beads is assumed to be unity, the same as that of other simple particles.

B. The sphere model

In literature, there are two DPD approaches that have been proposed for representing a sphere. The first is a smooth-sphere model[17] where the sphere and the fluid particle interact through an energy conserving Lennard-Jones two-body potential. This approach has been extensively used for simulations of simple shapes such as spheres, disks, and cylinders. The other representation, often referred to as the rough-sphere model,[20] involves representing the sphere by locally freezing the DPD particles to form a solid body. Although, this model does not result in a perfectly smooth

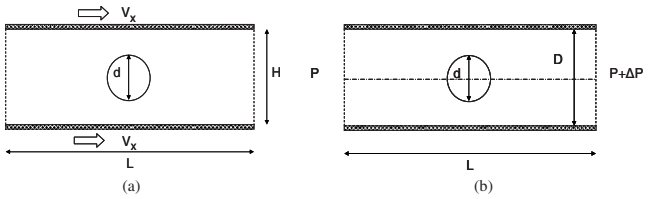

FIG. 2. Computational domain: (a) channel of infinite extent and (b) cylindrical channel.

sphere, a relatively smooth surface can be reproduced by choosing appropriate locations of the frozen particles. A uniform simple cubic arrangement of the particles inside the sphere is considered in this work. The interaction between the sphere and the fluid occurs via particle-particle interaction. A disadvantage of the approach is that it allows penetration of some fluid particles into the sphere. This can be prevented by applying a specular reflection at the sphere surface. When implementing the specular reflection model, if the fluid particle collides with the boundary of the sphere, the component of the particle's momentum that is normal to the surface of the sphere is reversed, while the component that is parallel to the surface is conserved.[19] Chen *et al.*[20] showed that implementing the specular reflection does not result in any significant improvement when calculating the drag force $\mathbf{F}_D$ on the sphere. In the present work, the rough-sphere model with no specular reflection at boundary is employed.

III. MODEL IMPLEMENTATION

In this section, the implementation and validation of the model for channel flow simulation will be discussed. In this work, channels of infinite extent and cylindrical channels will be employed. The computational domains for the simulations are shown in Fig. 2, where L is the length of the channel, d is the diameter of the sphere, H is the width of the channel, and D is the diameter of the cylindrical channel. The domain consists of three elements: the Newtonian fluid, the sphere, and the wall. The initial configuration of the DPD particles constituting the Newtonian fluid is a uniform simple cubic arrangement of particles. These particles are initialized with random velocity distribution with a zero mean velocity, corresponding to the system temperature. The boundary conditions that are employed for simulation of a channel of infinite extent include a frozen wall of DPD particles in the x-z plane while periodic boundary conditions are employed in the x- and z-directions. Following the work of Duong-Hong *et al.*,[25] the wall is represented by two layers of frozen particles. The no-slip condition at the upper and lower walls is implemented by using the bounce-back reflection method.[26] The shear flow in the channel is simulated by giving the wall particles a uniform velocity (V_x) in the x-direction. In the case of cylindrical channels, periodic boundary conditions are applied in the x-direction and bounce-back reflection is applied at channel walls to satisfy the no-slip condition. In cylindrical channels, pressure-driven flow is simulated by applying a uniform body force in the x-direction.

TABLE I. Parameters for drag flow simulations.

Parameter	Value in DPD units	Equation No.
Fluid-fluid repulsion coefficient (a_{fluid})	18.75	(3)
Wall-wall repulsion coefficient (a_{wall})	5.0	(3)
Fluid-wall repulsion coefficient (a_{ij})	9.68	(3)
Cutoff radius (r_c)	1.0	(3) and (8)
Dissipative force amplitude (γ)	4.5	(4) and (7)
Random force amplitude (σ)	3.0	(5) and (7)
System temperature (k_BT)	1.0	(7)
Density (ρ_f)	4.0	(15)–(17)
Sphere diameter (d)	3.0	(16)–(18)

A. Simulation parameters

The values of the simulation parameters employed in this study are listed in Table I. The computational domain for the shear flow has 120 000 fluid particles $(120\times20\times50)$ and 24 000 wall particles. The sphere is represented by 56 particles and has a diameter of 3 units. The size of the computational domain is chosen so as to hydrodynamically decouple the periodic images of the sphere. The channel walls have no effect on the interaction between the fluid flow field and the sphere. Chen *et al.*[20] conducted simulations to decouple the periodic images and concluded that the computational domain should be selected such that $\Delta X/d \geq 30$, $\Delta Y/d \geq 3.3$, and $\Delta Z/d \geq 14$; d is the diameter of the sphere and ΔX, ΔY, and ΔZ are dimensions of the domain in the x-, y-, and z-directions. Simulations were carried out to study the effect of channel dimensions on hydrodynamic decoupling. In the case of cylindrical channels, Fig. 3 shows that hydrodynamic decoupling exists in the x-direction. It can be seen that as $\Delta X/d$ approaches 25, the drag force becomes a constant and the spheres do not influence their periodic images. The channel length is fixed at 75.6 units (120 particles in the x-direction) and the diameter of the channel is varied to study the effect of the aspect ratio on $\mathbf{F}_D$. The amplitudes of dissipative and random forces (γ and σ) are selected to satisfy Eq. (7). The system temperature is selected so that the dissipative component of viscosity ν_D of the DPD fluid is

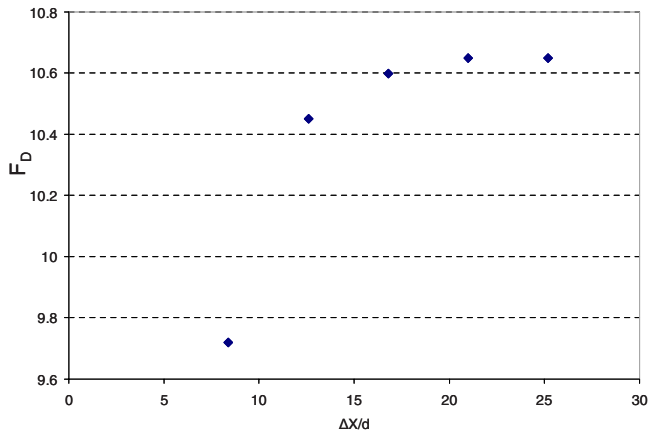

FIG. 3. (Color online) Hydrodynamic decoupling in the axial direction in a cylindrical channel.

greater than the kinetic component ν_K in the following equation obtained from the analysis of Groot and Warren:[23]

$$\nu_K = \frac{2\pi\gamma\rho r_c^5}{1575},$$

$$\nu_D = \frac{45k_BT}{4\pi\gamma\rho r_c^3}, \tag{13}$$

where γ is the amplitude of the dissipative force, ρ is the number density of DPD particles, r_c is the cutoff radius, k_B is the Boltzmann constant, and T is the system temperature. This assures that the Schmidt number (Sc) for the system is much greater than 1. This would mean that the fluid being simulated has the properties of a liquid. The fluid, the wall and the sphere are assumed to have an equal density of 4 units. The fluid-fluid repulsion coefficient a_{fluid} in Eq. (3) is obtained as 18.75 assuming that the fluid is water and matching the isothermal compressibility.[23] Following Chen *et al.*[20] the wall particle repulsion coefficient in Eq. (3), a_{wall}, is selected as 5. The interaction between the fluid and wall particles occurs via a repulsion coefficient $a_{ij}=\sqrt{a_{\text{fluid}}a_{\text{wall}}}$. This repulsion coefficient is used in Eq. (3) to simulate the interparticle forces between the wall particles and fluid particles.

In the simulations, all the parameters utilized are nondimensional and scaled by DPD units. The cutoff radius r_c is set to 1 and represents the length scale of the system. The mass of each DPD particle is set as unity. The system temperature used in these simulations is $k_BT=1.0$ (see Table I). The definition of Schmidt number Sc for the DPD system[23] is

$$\text{Sc} = \frac{1}{2} + \frac{(2\pi\gamma\rho r_c^4)}{70875k_BT}^2. \tag{14}$$

Hence, as the density of the system increases, Sc of the fluid increases. For the parameters selected in this work, Sc for all the simulations is 0.68 which is a couple of orders of magnitude smaller than a typical liquid. Such a small value implies that particles are diffusing as fast as momentum in a fluid. Note that liquidlike Schmidt numbers can be achieved by selecting the appropriate set of parameters. In this work, the parameters were selected to match those of Ref. 20.

IV. RESULTS AND DISCUSSION

The model is assessed for accuracy by computing the drag coefficient C_D for a sphere placed in a uniform shear flow in a rigid channel, as shown in Fig. 2(a), and comparing it with prior results. Figures 4 and 5 show the local fluid density and velocity distributions, respectively, in the near-sphere region for a case with Re=5.63. Recall that the sphere diameter is 3. The local fluid density and velocity distributions are calculated by considering a cubical region of $0.4\times12.6\times0.4$ (with the x-z face centered along $x=0$ and $z=0$ and y ranging from -6.3 to 6.3) and then dividing this region into 29 cells where each cell has a size of $0.4\times0.46\times0.4$. This is the same size employed by Chen *et al.*[20] Averaging is carried out over 8×10^4 time steps to reduce the fluctuations caused due to small sampling cell sizes. As discussed in Sec. III A, since a rough-sphere model is employed, the fluid particles penetrate the sphere. Notice from Fig. 4 that, as a result of penetration, the density of *fluid particles* within the sphere is about 25% of the density of the fluid. This value is comparable to that reported by Chen *et al.*[20] This penetration does not have a noticeable on the results as will be discussed later, and pointed out by Chen *et al.*[20] A specular reflection model can be employed to remove this artifact. However, it also has an artificial reversal of the normal velocity of the particle which can introduce errors in the computation of $\mathbf{F}_D$. Computations carried out with the specular reflection model by Chen *et al.*[20] show that there is no advantage in using it for calculation of $\mathbf{F}_D$ and, in fact, simulations with no explicit treatment of fluid-sphere boundary provide better accuracy than the specular model under similar conditions.

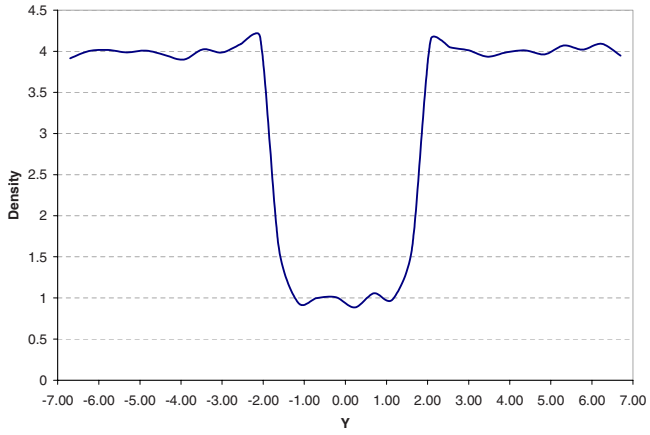

FIG. 4. (Color online) Density distribution in the y-direction along a line that passes through the center of the sphere (Re=5.63).

Figure 5 shows the velocity distribution in the near-sphere region. There are significant fluctuations in the fluid velocity, especially within the sphere, which are caused due to the fact that the number of particles in the cell employed for ensemble-averaging is too small. Since we are utilizing a very small cell volume, 80 000 time steps are still not sufficient to obtain a smooth velocity profile. In fact, Chen *et al.*[20] conducted averaging over a million time steps and still ob-

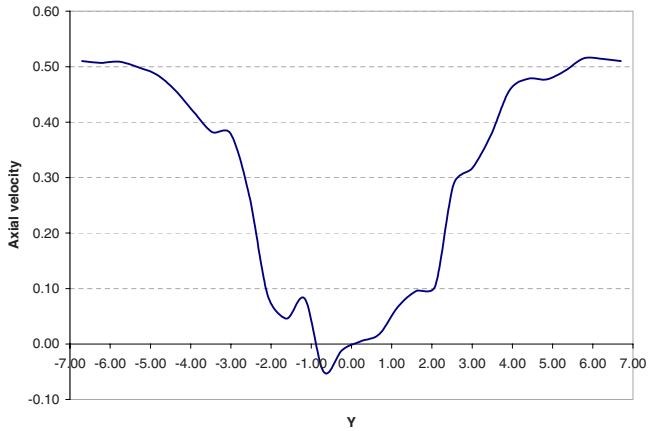

FIG. 5. (Color online) Velocity distribution (V_x) in the y-direction along a line that passes through the center of the sphere (Re=5.63).

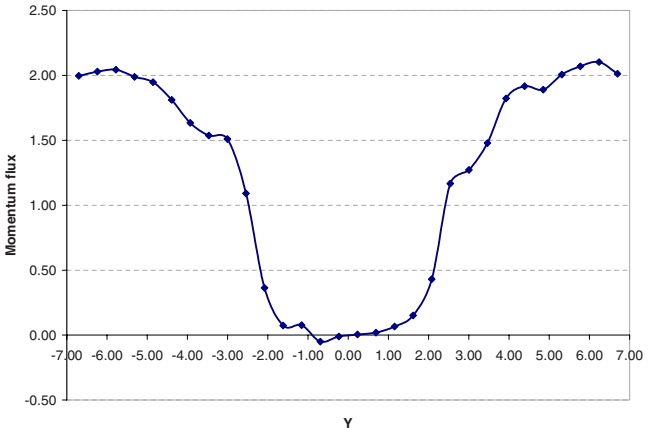

FIG. 6. (Color online) Momentum flux distribution (ρV_x) in the y-direction along a line that passes through the center of the sphere (Re=5.63).

served fluctuations. However, it can be seen in Fig. 5 that the velocity is uniform away from the sphere and it drops as we approach the sphere. In order to assess the influence of the fluid particles which penetrate the sphere, a local distribution of the momentum flux per unit area has been plotted in Fig. 6. Momentum flux is defined as the product of the axial velocity and the number density of the fluid. It can be observed that the momentum of the fluid particles inside the sphere is a couple of orders of magnitude lower than the bulk flow, and hence these particles do not have a significant effect on the hydrodynamic behavior of the fluid.

The sphere is kept stationary as its position is not updated by integrating the equations of motion. There is some penetration of fluid particles inside the sphere. Note, however, that the position of these particles is updated. Hence, the number of fluid particles inside the sphere will attain an equilibrium concentration when the number entering equals the number leaving. Also, since the cutoff radius for interaction is smaller than the diameter of the sphere, the primary interaction between sphere and fluid occurs through the particles on the surface of the sphere. Hence, the interaction of fluid particles inside the sphere with the fluid particles outside the sphere is not significant.

A. Calculation of drag force

In the flow of a Newtonian fluid over a solid sphere, the drag is the component of the net hydrodynamic force in the direction of flow. The drag force $\mathbf{F}_D$ can be modeled as

$$\mathbf{F}_D = \tfrac{1}{2} C_D A \rho_f \mathbf{U}|\mathbf{U}|, \tag{15}$$

where C_D is the drag coefficient, A is the cross-sectional area perpendicular to the flow, ρ_f is the density of the fluid, and $\mathbf{U}$ is the velocity of the sphere relative to the fluid. In the case of flow over a sphere, Eq. (15) becomes

$$\mathbf{F}_D = \tfrac{1}{8} C_D \pi d^2 \rho_f \mathbf{U}|\mathbf{U}|, \tag{16}$$

where d is the diameter of the sphere. At low Reynolds numbers, i.e., for creeping flow conditions, where the inertial forces become negligible, $\mathbf{F}_D$ is given by[27]

$$\mathbf{F}_D = 3\pi\mu d\mathbf{U}, \tag{17}$$

where μ is the dynamic viscosity of the fluid. The Reynolds number of such a flow can be defined as

$$\mathrm{Re} = \frac{\rho_f |\mathbf{U}| d}{\mu}. \tag{18}$$

Hence C_D for creeping flows is given by

$$C_D = \frac{24}{\mathrm{Re}}. \tag{19}$$

In systems where inertial effects can no longer be neglected, correlations for $\mathbf{F}_D$ are determined from experiments. Brown and Lawler[28] employed correlations that they developed from the experimental data of Fidrelis and Whitmore[29] and proposed the following experimental correlation for the range of Reynolds number considered ($\mathrm{Re} \leq 2 \times 10^5$):

$$C_D = \frac{24}{\mathrm{Re}}(1 + 0.150\ \mathrm{Re}^{0.681}) + \frac{0.407}{1 + (8710/\mathrm{Re})}. \tag{20}$$

In order to assess the accuracy of the code, a parametric study has been carried out to determine the variation of C_D with Re. The approximate range of Re considered is 1–10. The model parameters and simulation conditions for the following simulations are listed in Table I and discussed above. In these simulations, the values of λ tends to zero and there is no effect of the wall on the drag force acting on the sphere. The dynamical viscosity for the fluid can be calculated from Eq. (13) and is 1.083 for the simulation. The fluid used in this work is the same as that used by Chen *et al.*[20] and Fan *et al.*[30] The dynamic viscosity of the DPD fluid was estimated to be about 1.077 by Fan *et al.* by fitting numerical results of flow profiles to known profiles. Notice that there is good agreement between the two results, i.e., from the numerical simulations and Eq. (13). After the flow inside the channel has reached steady state, $\mathbf{F}_D$ is calculated by summing over the net force exerted on the sphere particles by the fluid particles in the x-direction. The computed $\mathbf{F}_D$ is also allowed to relax to a steady value. It is necessary to do this because the particles are initialized with random velocities corresponding to a system temp of 1.0. The system has to reach a steady flow profile before averaging can start. In Poiseuille flow simulations, it takes approximately 20 000 time steps for the flow to reach the parabolic flow profile. The initial flow development phase is not considered when estimating C_D. Equation (15) is employed to calculate C_D. Figure 7 shows the variation of C_D. Results obtained from Eqs. (19) and (20) are also shown for comparison. Since the inertial effects cannot be neglected in this system due to the presence of relatively high Re, the results deviate from Eq. (19). However, it can be observed that the agreement between the results and the Brown and Lawler[28] experimental correlation is reasonable; quantitative differences are within 3%. It is interesting to compare the quantitative results with those of Chen *et al.* Consider the case where Re is approximately 6. The drag coefficient in Fig. 7 for this Re is about 4, and this is comparable to the value reported by Chen *et al.*

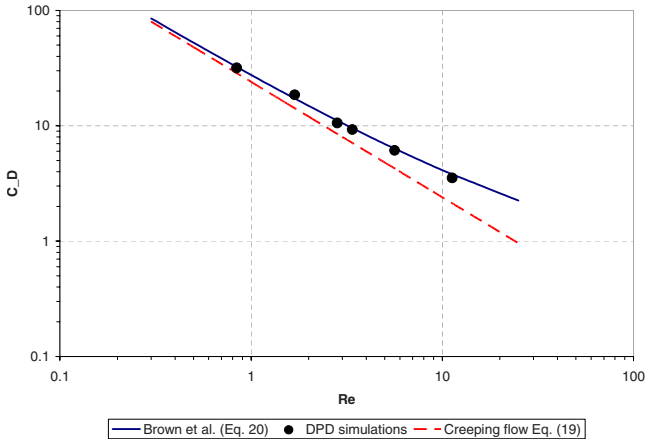

FIG. 7. (Color online) Variation of drag coefficient C_D with Reynolds number.

B. Flow across a sphere in cylindrical channels

The model is now extended to compute flow in a cylindrical channel. Note that this flow differs from the one above in that it is constrained by the boundary. In Sec. IV A, although a channel or slit of infinite width was simulated, the domain size was selected to ensure that the walls and the periodic images do not influence the drag coefficient, i.e., free flow was simulated. However, in constrained flows, the channel walls have an influence on the drag force $\mathbf{F}_D$. The dependence of the $\mathbf{F}_D$ on the channel geometry can be studied by varying an aspect ratio λ, defined as the ratio of the sphere diameter d to the channel diameter D, and evaluating its influence on $\mathbf{F}_D$. Figure 2(a) shows the computational domain for flow past a sphere in a cylindrical channel. The flow is driven by a constant body force in x-direction in the DPD model. The parameters used are given in Table I.

Figure 8 shows the radial density distribution of particles from the center of the sphere for a simulation with λ=0.19 and Re=4.92. The length L of the channel is 75.6 DPD units whereas D is 15.75 units. The sphere has a diameter d of 3 units and is represented by 56 particles arranged in a cubic

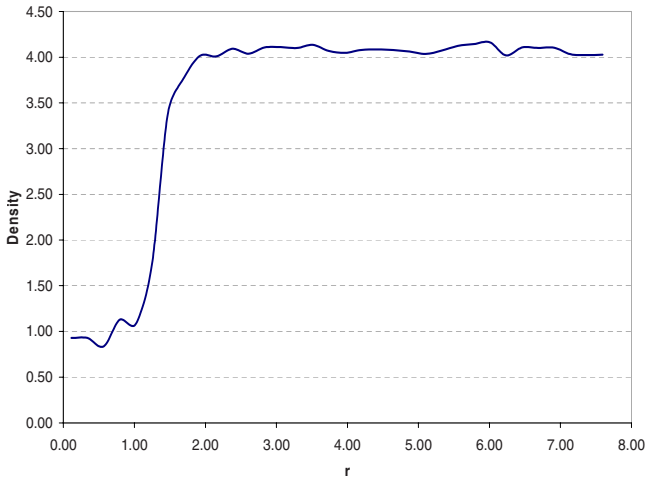

FIG. 8. (Color online) Density distribution in the y-direction along a line that passes through the center of the sphere (λ=0.19 and Re=4.92).

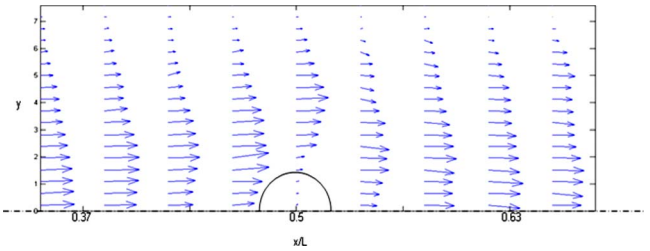

FIG. 9. (Color online) Velocity vector plot (λ=0.19 and Re=4.92).

lattice. Chen *et al.*[20] found that the drag coefficient did not change with change in d; they obtained a similar density profile with a sphere of diameter 6, i.e., the fluid density within the sphere was about 25% of the ambient. Figure 9 shows the velocity vector plots for a computation with Re =4.92. Figure 10 shows axial velocity (V_x) profiles at different sections in the channel. The center of the sphere is at x/L of 0.5. It is evident from the figures that the flow field is noticeably modified near the sphere but settles into a Poiseuille flow pattern farther downstream. The particle treatment results in some spurious velocities inside the sphere, for reasons discussed earlier. However, as demonstrated earlier in the rectangular channel simulations, these are relatively small, and when the product of the number density of particles and the velocity, i.e., the momentum flux, is considered, the effects are small.

In order to study the influence of the wall on $\mathbf{F}_D$, simulations are carried out for several values of the aspect ratio λ. Figure 11 shows the variation of C_D with Re for three λ: 0.19, 0.25, and 0.33. The simulations are restricted to lower values of λ since higher values will result in significant pressure difference between downstream and near-sphere regions which, in turn, can lead to leakage into the sphere with the boundary treatment adopted here. Note that the simulations in this work are conducted in the incompressible regime. The sound velocity can be estimated by $c=\sqrt{\partial p/\partial \rho|_T}$ based on the virial expression for the pressure.[23] The Mach number (Ma) is less than 0.3. At higher λ, compressibility effects come into play and the DPD model is unable to accurately model these effects. It can be observed in Fig. 11 that as we move to smaller λ, C_D at a given Re decreases, and the C_D versus λ curve approaches that for the free-flow condition. The free-flow condition corresponds to the λ=0 curve which can ei-

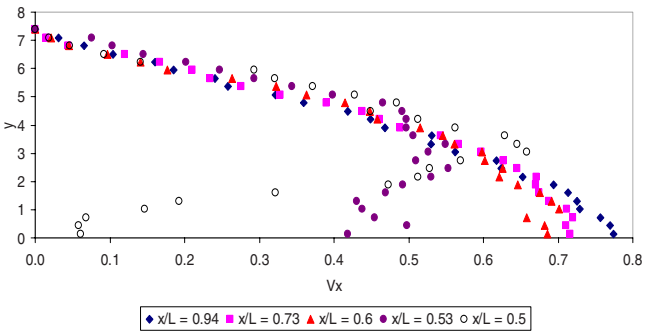

FIG. 10. (Color online) Axial velocity profiles at several channel sections, downstream of the sphere (λ=0.19 and Re=4.92).

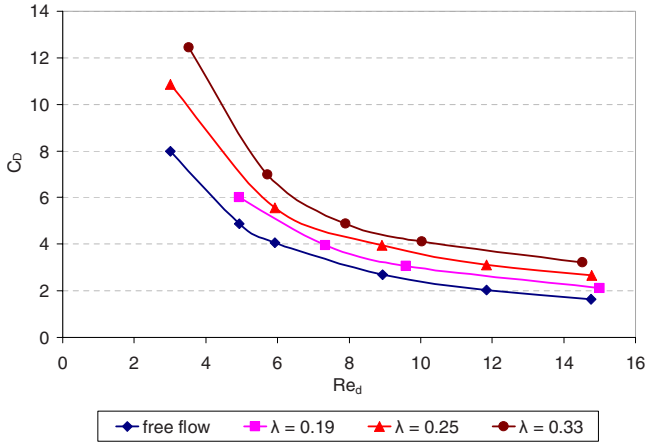

FIG. 11. (Color online) Variation of C_D with Re for several aspect ratios.

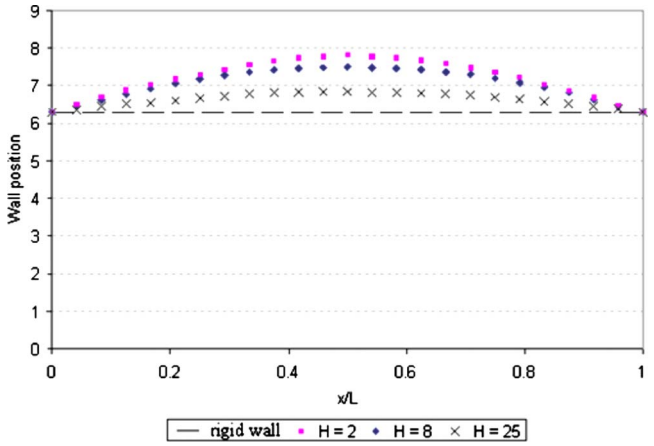

FIG. 13. (Color online) Deformation of elastic wall for several H when $\lambda=0.25$ and $r_{max}=3.0$.

ther be calculated from theoretical expressions for free flow or numerical simulations in a rectangular channel as carried out in Sec. III. Since a larger λ implies that there is larger resistance to the flow past the sphere, the simulation results conform to the expected trends.

It is interesting to observe that the results of Fig. 11 imply that the drag coefficient scales with the nondimensional parameters Re and λ. This is known for predictions from continuum hydrodynamics, but it is not apparent for DPD simulations which are more applicable for submicron flows. Additional simulations were performed to assess if the problem can indeed be completely specified in terms of these dimensionless groups. In the simulations in Fig. 11, the system temperature K_BT and the kinematic viscosity ν were 1 and 0.270, respectively. Consider the case with Re=6.0 in Fig. 11. This Re can be obtained by selecting a different set of K_BT and ν values. In fact, with $K_BT=0.79$ and $\nu=0.241$, Re is approximately 6. With these values, the simulations were repeated when $\lambda=0.25$ and 0.33. The maximum difference in drag coefficient between the original case in Fig. 11 and these two new cases was less than 5%. These results are in agreement with the prediction from continuum hydrodynamics that the problem can be completely specified in terms of the dimensionless groups.

Figure 12 shows the variation of C_D with λ for Re

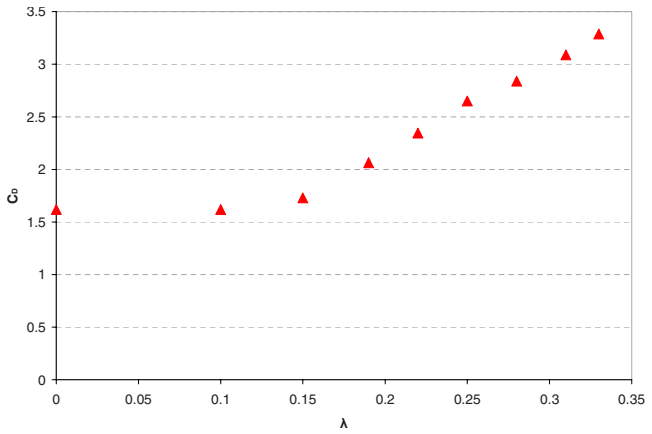

FIG. 12. (Color online) Variation of C_D with aspect ratio (Re ~ 15).

~ 15. Since Re is calculated on the basis of the average flow velocity which is postprocessed after the simulation is complete, there is 3%–5% variability in the Re which introduces some variability/error in the computed C_D. This variability notwithstanding, it is evident from Fig. 12 that initially there is no change in C_D when increasing λ from 0 to 0.1 as the walls are hydrodynamically decoupled from the sphere. This means that the sphere is unable to feel the presence of the channel walls and, hence, the free flow C_D is recovered. However, on further increasing λ to 0.16, a slight increment in C_D is observed and continuing increase in λ causes significant increase in C_D as the sphere is no longer hydrodynamically decoupled from the wall.

C. Flow across a sphere in compliant channels

The influence of the elasticity of the wall on the drag force $\mathbf{F}_D$ is now studied. As discussed in Sec. II, the nonlinear elastic behavior of the wall is modeled using FENE bead-chain springs. The model has two parameters [see Eq. (12)]: H, the amplitude of the spring force, and r_{max}, the maximum extension of the spring, that can be used to vary the elasticity of the wall. The length L of the channel is 75.6 DPD units and the channel diameter D is 12.4 units. The maximum extension of the spring is set to 3.0. Figure 13 shows the deformation of the wall as a consequence of the variation of H for $\lambda=0.25$ and $r_{max}=3.0$. Since the position of the wall particles fluctuate as a result of the randomness in the DPD model, the wall position is determined by estimating the mean radial distance of the wall particles at different axial locations. As H increases, the wall becomes more rigid because there is a stronger force acting on the spring to revert it back to its original shape. Figures 14 and 15 show the variation of drag coefficient with Re for $\lambda=0.25$ and $\lambda=0.33$, respectively. Note that $r_{max}=3.0$ in both figures. It can be observed that as the amplitude of the spring force increases, there is an increase in C_D. Now, a more elastic wall will deform more easily in response to the fluid flow. Hence, it imposes less resistance to the fluid flow. As a result, $\mathbf{F}_D$ decreases. Another way to think of this is that the "effective" λ at the sphere location is smaller when the wall is more

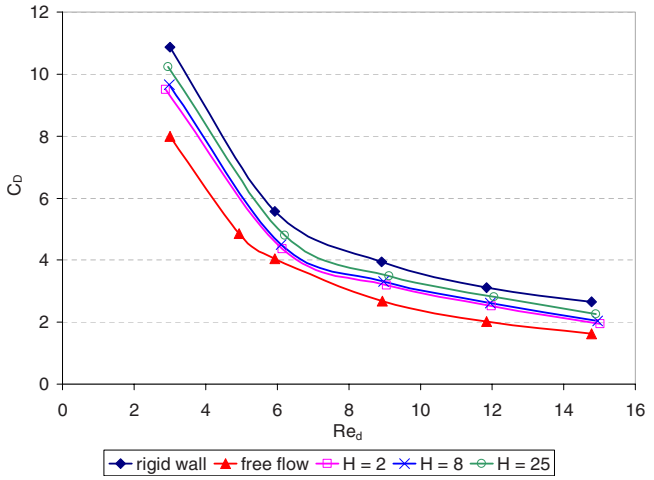

FIG. 14. (Color online) Variation of drag coefficient with Re for several H values when $\lambda=0.25$.

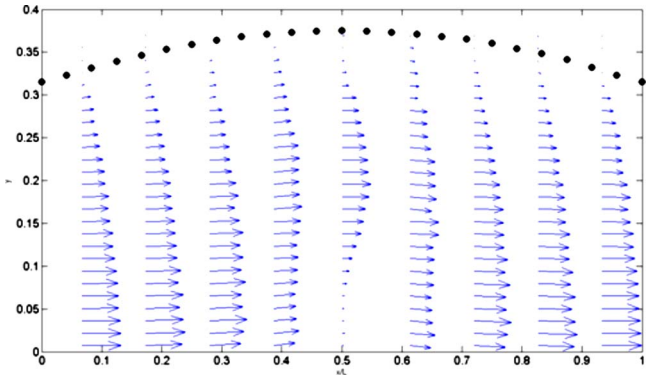

FIG. 16. (Color online) Velocity vector plot (Re=6.1, $H=8$, $\lambda=0.25$, and $r_{max}=3.0$).

elastic. Figure 16 shows the velocity vector plot for $H=2$, $r_{max}=3.0$, and $\lambda=0.25$ at Re=6.1. The wall position for these conditions is overlaid on vector plot and the sphere is located at $x/L=0.5$. The flow field is clearly modified near the sphere, but it relaxes back to a Poiseuille flow profile downstream. There is, however, a variation of the cross-sectional area of the channel due to the elastic behavior of the walls. Hence, there is a net flow in the radial direction even at far upstream and downstream locations of the channel.

Figure 17 shows the variation of C_D with Re for different maximum extension (r_{max}) values of the spring. As the maximum extension increases, the effective value of λ decreases in the near-sphere region. As a result, the curve shifts toward the free-flow asymptote for all values of Re. To illustrate this point further, Fig. 18 shows the variation of C_D with r_{max} ($\lambda=0.25$, $H=6.0$, and Re=8.97). As r_{max} increases, the walls become more elastic as the FENE chains connecting the various wall particles can extend further. Hence, the walls offer less resistance to the fluid flow and eventually, at steady state, lead to a lower $\mathbf{F}_D$. However, as r_{max} approaches r_C (which is unity in the current set of simulations), the denominator in Eq. (12) approaches zero and this results in a large spring force. Under these conditions, the wall behaves like a rigid wall. It can be seen in Fig. 17 that the $r_{max}=1$ curve almost overlaps with the rigid wall curve. It must be noted, however, that r_{max} cannot be set exactly to unity as this causes numerical instability due to the large forces. Hence, Figs. 17 and 18 actually show the results for $r_{max}=1.02$. It can also be observed in Fig. 18 that when the r_{max} value is large, the C_D reaches an asymptotic value as the elasticity of the wall is now primarily dominated by amplitude of the spring (H) instead of the maximum spring extension (r_{max}).

V. SUMMARY AND CONCLUSIONS

In this work, a DPD-based model has been developed to simulate flow past a sphere in cylindrical compliant channels. The model has been assessed for accuracy by comparing predicted coefficient of drag results for spheres with prior results. Agreement is obtained within 3%. The model is then extended to simulate flow past spheres in *compliant cylindrical channels*. The effect of the aspect ratio λ, defined as the ratio of sphere diameter to channel diameter, on the drag coefficient C_D is studied and it is shown that C_D increases as λ increases. Also, below a certain value of λ, the walls become hydrodynamically decoupled from the sphere and the system behaves as in a free-flow system. The effect of the

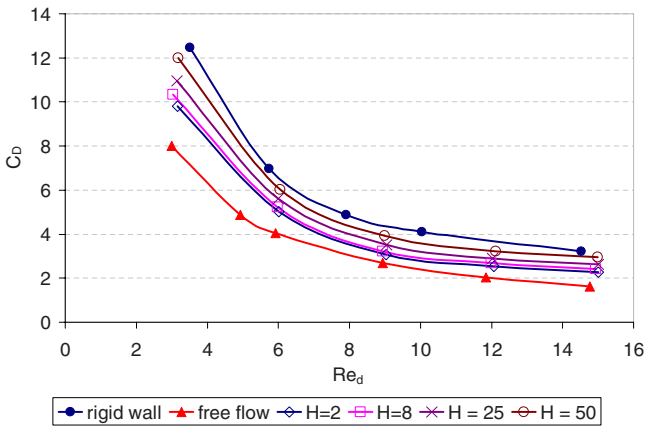

FIG. 15. (Color online) Variation of drag coefficient with Re for several H values when $\lambda=0.33$.

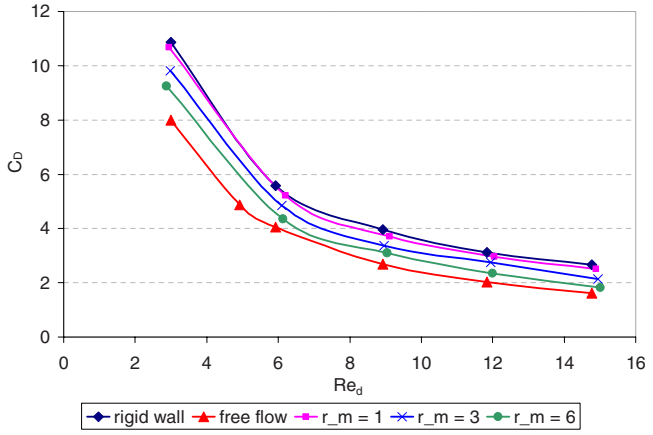

FIG. 17. (Color online) Variation of drag coefficient with Re for several r_{max} values when $\lambda=0.25$ and $H=6.0$.

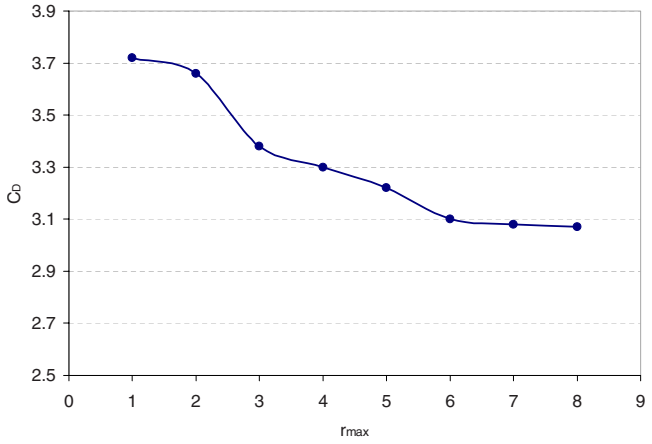

FIG. 18. (Color online) Variation of drag coefficient with r_{max} ($\lambda=0.25$ and $H=6.0$).

elasticity of the walls on the drag coefficient is also studied. The elastic behavior is modeled using FENE chain model which has two model parameters: H, the spring constant, and r_{max}, the maximum permissible length of one chain segment. Increasing H decreases elasticity and increasing r_{max} increases elasticity. The influence of an increase in elasticity is to decrease the value of C_D because the outward movement of the wall in the region near the sphere effectively reduces the value of λ.

ACKNOWLEDGMENTS

Computational resources for this work were provided by the Rosen Center for Advanced Computing at Purdue.

[1]U. Frisch, B. Hasslacher, and Y. Pomeau, "Lattice-gas automata for Navier-Stokes equation," Phys. Rev. Lett. **56**, 1505 (1986).
[2]S. Wolfram, "Cellular automaton fluids: Basic theory," J. Stat. Phys. **45**, 471 (1986).
[3]A. Ladd, "Numerical simulations of particulate suspensions via a discretized Boltzmann equation. Part II. Numerical results," J. Fluid Mech. **271**, 311 (1994).
[4]P. G. Ciarlet, *The Finite Element Method for Elliptic Problems* (North-Holland, Amsterdam, 1978).
[5]M. A. A. Spaid and F. R. Phelan, Jr., "Lattice Boltzmann methods for modeling microscale flow in fibrous porous media," Phys. Fluids **9**, 2468 (1997).
[6]C. Y. Lim, C. Shu, X. D. Niu, and Y. T. Chew, "Application of lattice Boltzmann method to simulate microchannel flows," Phys. Fluids **14**, 2299 (2002).
[7]P. J. Hoogerbrugge and J. M. V. A. Koelman, "Simulating microscopic hydrodynamic phenomena with dissipative particle dynamics," Europhys. Lett. **19**, 155 (1992).
[8]P. Espanol, "Hydrodynamics from dissipative particle dynamics," Phys. Rev. E **52**, 1734 (1995).
[9]A. Satoh and T. Majima, "Comparison between theoretical values and simulation results for the dissipative particle dynamics method," J. Colloid Interface Sci. **283**, 251 (2005).
[10]E. S. Boek, P. V. Coveney, H. N. W. Lekkerkerker, and P. van der Schoot, "Simulating the rheology of dense colloidal suspensions using dissipative particle dynamics," Phys. Rev. E **55**, 3124 (1997).
[11]A. G. Schlijper, P. J. Hoogerbrugge, and C. W. Manke, "Computer simulations of dilute polymer solutions with dissipative particle dynamics," J. Rheol. **39**, 567 (1995).
[12]P. V. Coveney and K. E. Novik, "Computer simulations of domain growth and phase separation in two-dimensional binary immiscible fluids using dissipative particle dynamics," Phys. Rev. E **54**, 5134 (1996).
[13]J. N. A. R. T. Clark, M. Lal, and P. B. Warren, "Mesoscopic simulation of drops in gravitational and shear fields," Langmuir **16**, 6342 (2000).
[14]A. Tiwari and J. Abraham, "Dissipative particle dynamics simulations of liquid nanojet breakup," Microfluid. Nanofluid. **4**, 227 (2008).
[15]A. Tiwari, H. Reddy, S. Mukhopadhyay, and J. Abraham, "Simulations of liquid nanocylinder breakup with dissipative particle dynamics," Phys. Rev. E **78**, 016305 (2008).
[16]E. S. Boek and P. van der Schoot, "Resolution effects in dissipative particle dynamics," Int. J. Mod. Phys. C **9**, 1307 (1998).
[17]W. Dzwinel and D. A. Yuen, "A two-level, discrete-particle approach for simulating ordered colloidal structures," J. Colloid Interface Sci. **225**, 179 (2000).
[18]M. Whittle and E. Dickinson, "On simulating colloids with dissipative particle dynamics: Issues and complications," J. Colloid Interface Sci. **242**, 106 (2001).
[19]J. M. Kim and R. J. Phillips, "Dissipative particle dynamics simulation of flow around spheres and cylinders at finite Reynolds numbers," Chem. Eng. Sci. **59**, 4155 (2004).
[20]S. Chen, N. Phan-Thien, B. C. Khoo, and X. J. Fan, "Flow around spheres by dissipative particle dynamics," Phys. Fluids **18**, 103605 (2006).
[21]S. Chen, N. Phan-Thien, X. J. Phan, and B. C. Khoo, "Dissipative particle dynamics simulation of polymer drops in periodic shear flow," J. Non-Newtonian Fluid Mech. **118**, 65 (2004).
[22]P. Espanol and P. B. Warren, "Statistical mechanics of dissipative particle dynamics," Europhys. Lett. **30**, 191 (1995).
[23]R. D. Groot and P. B. Warren, "Dissipative particle dynamics: Bridging the gap between atomistic and mesoscopic simulations," J. Chem. Phys. **107**, 4423 (1997).
[24]A. Tiwari, "DPD for two-phase flows," Ph.D. thesis, Purdue University, 2006.
[25]D. Duong-Hong, N. Phan-Thien, and X. J. Fan, "An implementation of no-slip boundary condition in DPD," Comput. Mech. **35**, 24 (2004).
[26]M. Revenga, I. Zuniga, and P. Espanol, "Boundary conditions in dissipative particle dynamics," Comput. Phys. Commun. **121–122**, 309 (1999).
[27]G. K. Batchelor, *An Introduction to Fluid Dynamics* (Cambridge University Press, Cambridge, 1967).
[28]P. P. Brown and D. F. Lawler, "Sphere drag and settling velocities revisited," J. Environ. Eng. **129**, 222 (2003).
[29]V. Fidleris and R. L. Whitmore, "Experimental determination of the wall effect for spheres falling axially in cylindrical vessels," Br. J. Appl. Phys. **12**, 490 (1961).
[30]X. J. Fan, N. Phan-Thien, T. Y. Ng, H. Wu, and D. Xu, "Microchannel flow of macromolecular suspension," Phys. Fluids **15**, 11 (2003).